Integrating Topographic Continuity and Lake Recession Dynamics for Improved Bathymetry Mapping from DEMs

Fukun Tao[1], Yong Wang[1], Yinghong Jing[1], Xiaojun She[1], Shanlong Lu[2], Yao Li[1]

[1] Chongqing Jinfo Mountain Karst Ecosystem National Observation and Research Station, School of Geographical Sciences, Southwest University, Chongqing 400715, China

[2] Aerospace Information Research Institute, Chinese Academy of Sciences, Beijing 100094, China

Correspondence to: Yao Li (liyao7@swu.edu.cn)

Abstract. Accurate lake bathymetry is critical for advancing hydrological and biogeochemical research, yet large-scale and deep-water mapping remains constrained by cost challenges. While remote sensing techniques have been extensively employed for bathymetric mapping, their effectiveness is primarily limited to shallow waters due to the rapid attenuation of optical signals with increasing depth. To overcome this limitation, we propose a novel bathymetric mapping method that leverages topographic continuity to infer underwater terrain by simulated progressive lake recession. This approach relies solely on Digital Elevation Model (DEM) data, using shoreline topographic gradients to estimate depth, providing a robust alternative for regions where conventional surveying is impractical. Validation across 12 lakes on the Tibetan Plateau demonstrated promising accuracy, with an average normalized root-mean-square error of 19.08% for depth estimation and a mean absolute percentage error of 23.47% for lake volume. To evaluate the method's generalizability across diverse hydrological settings, it was applied to Lake Mead, United States, producing a bathymetric map with a correlation coefficient of 0.66 against in situ measurements. Overall, this study introduces a low-cost solution for bathymetric mapping in data-scarce regions, offering a valuable tool for assessing lake volume at regional and global scales.

1 Introduction

Lakes, covering approximately 2% of the global land surface, play a critical role in water resource assessments and water balance analyses (Råman Vinnå et al., 2021; Pekel et al., 2016). They act as essential mediators of water-energy exchanges and serve as sensitive indicators of climate change at both regional and global scales (Vinogradova et al., 2025). By directly influencing water resource equilibrium, lakes are integral to hydrological and ecological processes (Williamson et al., 2009). Bathymetric data and lake volume, two key physical parameters of lakes, are fundamental for various applications, including hydrodynamic modeling (Yoon et al., 2012; Durand et al., 2008), aquatic vegetation monitoring (Gong et al., 2021), water resource management (Li et al., 2023; Yang et al., 2021), and climate model evaluation (Woolway et al., 2020). Therefore, accurate measurements of lake depth and volume are essential for environmental conservation and sustainable

resource management. However, the efficiency of current bathymetric mapping technologies remains limited, substantially compromising the accuracy of lake volume estimates and restricting their practical applications. This underscores an urgent need for methodological innovations to advance lake depth estimation and volume prediction.

Traditional in situ bathymetric surveys rely on shipborne echo sounders, airborne LiDAR, and optical imaging sensors (Guo et al., 2022; Song et al., 2014; Smith and Sandwell, 1997). While these techniques provide high-resolution data, they are costly and impractical for large-scale lake assessments. Satellite remote sensing offers a cost-effective alternative for global inland water monitoring (Li et al., 2021b; Sheffield et al., 2018), yet accurately mapping underwater topography remains a significant challenge. Optical remote sensing is widely used for bathymetric mapping in shallow waters (Wang et al., 2024), but its effectiveness declines exponentially in deeper lakes due to limited light penetration (Roy and Das, 2022). Radar altimetry and Digital Elevation Models (DEMs) can capture topographic features but exhibit fundamental limitations in characterizing submerged terrain. Notably, prevailing global DEM products assign a fixed elevation value to water-covered areas, reflecting surface elevation rather than actual underwater topography (Li et al., 2021a; Yamazaki et al., 2017; Farr et al., 2007). Therefore, these products depict submerged terrain only in areas that became inundated after the time of observation, failing to deliver a comprehensive representation of lake bathymetry.

In recent years, the integration of satellite altimetry and optical remote sensing data has been increasingly employed to monitor the depth of inland waters (Li et al., 2019; Qiao et al., 2019; Duan and Bastiaanssen, 2013). Lake surface areas are typically derived from optical imagery, while water surface elevations are obtained from satellite altimetry data (Li et al., 2021a). By correlating the time series of the lake area with corresponding elevation measurements, area-elevation relationships can be established (Luo et al., 2021; Gao, 2015). Based on these relationships, lake volume is estimated through geometric volume calculation formulas tailored to specific lakes. For instance, Li et al. (2020) combined multi-source satellite altimetry data with Landsat imagery to establish area-elevation relationships, which were subsequently utilized to estimate dynamic reservoir depths. They further employed an extrapolation method to generate a complete bathymetric dataset. Although this method enables comprehensive bathymetric mapping, it depends on prior knowledge of the maximum lake depth as a constraint, limiting its applicability in regions where such information is unavailable.

Shoreline topography plays a crucial role in determining lake depth (Messager et al., 2016; Pistocchi and Pennington, 2006), as shoreline morphology and slope significantly impact water flow and sedimentation processes (Edmonds and Slingerland, 2010). Therefore, lake shoreline characteristics provide valuable input for lake depth estimation. Some studies have employed statistical models to analyze large datasets of known lake and reservoir depths. Nonlinear models based on surrounding topography have been developed to estimate average or maximum water depth, which is then used to calculate lake volume (Han et al., 2024; Cael et al., 2017; Messager et al., 2016). While such methods are generally reliable for large-scale studies due to compensatory effects of under- and over-estimations, uncertainties and biases remain substantial at local

or individual lake scales. Alternative approaches suggest that lake bathymetry can be inferred by extrapolating or interpolating from the surrounding terrain (Liu and Song, 2022; Getirana et al., 2018). Although these approaches can partially reconstruct underwater topography and estimate water volume, they often require prior in situ data, such as maximum lake depth, to constrain the results. Recently, several methods have been developed that eliminate the need for field measurements (Han et al., 2024; Fang et al., 2023; Zhu et al., 2019). Due to sediment accumulation, most modern lakes tend to develop deep-water zones with relatively flat bottoms (Zhang et al., 2018). Current DEM-based bathymetric mapping methods often truncate predictions when the estimated depth exceeds measured values (Zhang et al., 2016), leading to artificially flattened lake bottoms. However, such truncation fails to account for sedimentation processes and the variations in underwater topography caused by sediment accumulation.

To address these limitations, this study proposes a novel three-dimensional bathymetric mapping approach that utilizes DEM data to estimate lake depth and volume. The method leverages shoreline geometric features and topographic factors extracted from DEMs, while explicitly accounting for the physical processes of lake level recession (used here solely as a physical simulation in the reconstruction procedure, rather than implying an observed lake-level trend) and sediment deposition. By capturing the reshaping effects of sediment accumulation on lakebed morphology, this approach provides a more effective representation of underwater topography and supports improved lake volume estimates. Consequently, it offers a promising solution for generating bathymetric maps and estimating lake volume in natural lakes, even in regions with limited in situ data.

2 Data and Methods

2.1 Data

2.1.1 Digital Elevation Model datasets

NASADEM, an enhanced version of the Shuttle Radar Topography Mission (SRTM) DEM with a 1 arc-second (~30 m at the equator) spatial resolution, was used as the primary input dataset (Crippen et al., 2016). One of its key advantages for bathymetric mapping is its early acquisition time, which captures more exposed shoreline areas. Consequently, the DEM preserves geomorphic information from historically exposed shorelines and shallow lake margins, providing critical physical constraints for reconstructing present-day underwater topography and enabling more comprehensive lake depth estimation. It has been reprocessed using advanced algorithms to refine the original SRTM radar signal, incorporating precise elevation benchmarks primarily from the Ice, Cloud, and Land Elevation Satellite (ICESat) Geoscience Laser Altimeter System (GLAS) and the Advanced Spaceborne Thermal Emission and Reflection Radiometer (ASTER). Validation studies across the Tibetan Plateau have confirmed its high vertical accuracy, with a low root-mean-square error (RMSE) of 3.36 m in the validation area (Li et al., 2022). This dataset is publicly available through NASA's Earthdata portal

(https://www.earthdata.nasa.gov). To assess the impact of input data with different spatial resolutions on the simulation results, we incorporated two additional datasets: ALOS PALSAR DEM (12.5 m spatial resolution) and MERIT DEM (3 arc-second resolution, ~90 m at the equator). The ALOS PALSAR DEM data were obtained from the Japan Aerospace Exploration Agency (JAXA, https://www.eorc.jaxa.jp), and the MERIT DEM data were sourced from the International Centre for Water Hazard and Risk Management (ICHARM, https://hydro.iis.u-tokyo.ac.jp).

2.1.2 In situ bathymetric data

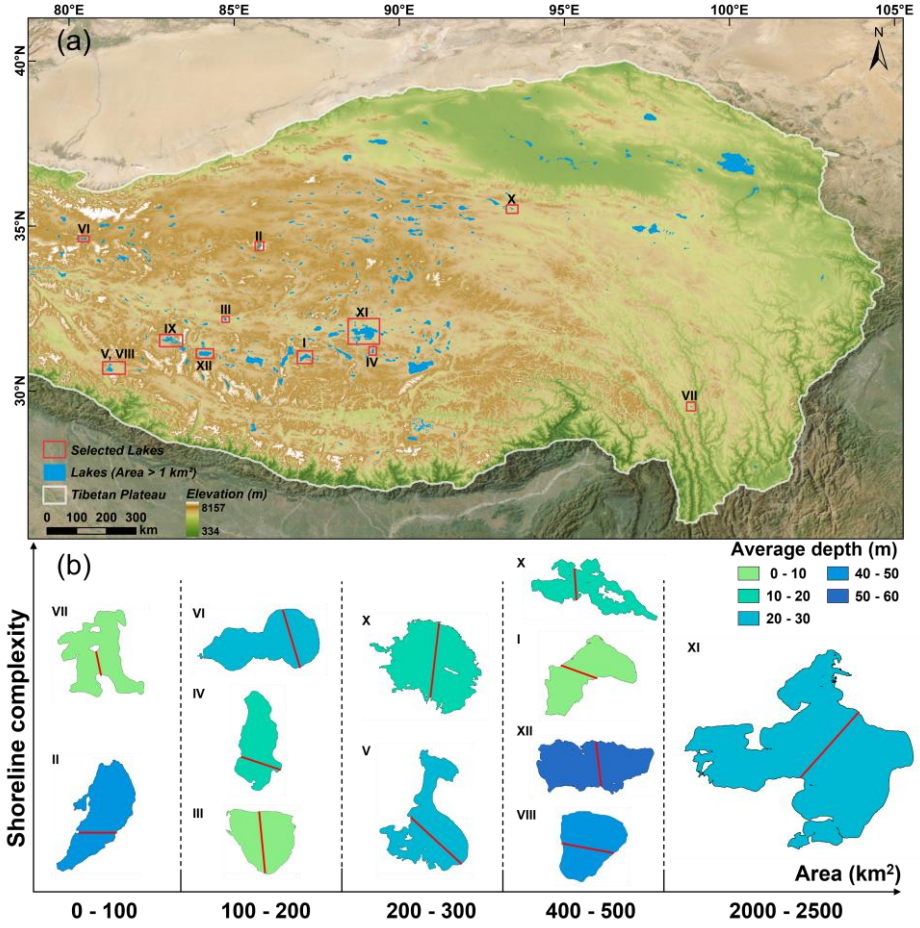

Figure 1: Overview of the 12 sample lakes on the Tibetan Plateau. (a) Distribution of lakes larger than 1 km² across the Tibetan Plateau, with the sample lakes in this study highlighted by red rectangles. (b) Shape characteristics of the 12 sample lakes, with colors indicating differences in mean lake depth. The red line denotes the transect used for validation in Fig. 8.

The in situ data were provided by the National Tibetan Plateau/Third Pole Environment Data Center (http://data.tpdc.ac.cn), which were collected using an echo sounder (Lowrance HDS5). Spatial interpolation was performed at a 30 m resolution, utilizing bathymetric points with longitude, latitude, and depth to generate in situ bathymetric maps. The shoreline shapefiles

were extracted at the zero-depth boundary (depth = 0 m) and used to calculate lake surface areas (Fig. S1). The selected lakes, which are evenly distributed across the Tibetan Plateau, exhibit diverse morphologies (Fig. S2). Their mean water surface elevations range from 4,299 m to 5,171 m, spanning an altitude difference of approximately 1,000 m. Most lakes have surface areas between 90 and 500 km², except for Siling Co, which is significantly larger at approximately 2,400 km². Maximum lake depths range from 4 m to 130 m, reflecting diverse bathymetric features and shoreline complexities. Detailed lake characteristics are presented in Table 1. Additionally, to assess the method's applicability across disparate hydrological contexts, a 30 m resolution bathymetric map of Lake Mead—an artificial reservoir—was obtained from the United States Geological Survey (USGS, https://www.usgs.gov/). This dataset includes information on post-impoundment sediment distribution within the lake. However, due to the limited coverage of the in situ bathymetric map, portions of the eastern region of Lake Mead were excluded from the analysis.

Table 1. Overview of the sample lakes on the Tibetan Plateau.

Lake ID	Measurement time	Lake name	Area (km²)	Average elevation (m)	Depth (m)	
					Average	Maximum
I	2018.09	Angzicuo	495.42	4693	9.70	18.83
II	2013.10	Buruocuo	92.67	5171	41.63	100.55
III	2019.07	Dongcuo	106.79	4397	2.06	3.99
IV	2019.07	Guomangcuo	113.63	4634	15.48	39.49
V	2017.09	Laangcuo	252.56	4571	21.90	49.19
VI	2015.09	Longmucuo	106.80	5009	25.27	67.52
VII	-	Mangcuo	19.39	4299	9.41	22.28
VIII	2017.09	Mapang Yongcuo	413.22	4585	41.62	79.45
IX	2017.09	Ngangla Ringco	498.06	4715	18.26	74.94
X	2019.11	Salt Lake	209.90	4469	13.13	32.78
XI	2014.08	Siling Co	2389.11	4539	22.07	52.50
XII	2012.06	Taro Co	487.49	4570	57.48	130.95

2.1.3 Comparative datasets

The estimated lake volumes were compared with those reported in three previous studies. GLOBathy is a recently developed global dataset that generates bathymetric maps based on maximum depth estimates, combined with the geometric and physical properties of water bodies from the HydroLAKES dataset (Khazaei et al., 2022). Han et al. (2024) adopted an

improved grid-based photon noise removal method to extract underwater photon signals from ICESat-2 data. By integrating statistical modeling with self-affine theory, they generated bathymetric maps of lakes and estimated lake volumes for lakes larger than 0.01 km² on the Tibetan Plateau. Fang et al. (2023) employed a trigonometric function as the fundamental shape of depth profiles and applied error correction based on different water level elevations to reduce the impact of sediment layers on simulation accuracy. The method was applied to 12 lakes on the Tibetan Plateau, and the results were included in the comparison.

2.2 Method

The bathymetric mapping algorithm consists of three main steps (Fig. 2). Parameter initialization: Key input parameters for underwater elevation estimation, including the water mask and shore slope, were extracted from the updated SRTM Water Body Data (SWBD) and the NASADEM elevation bands. The water mask defined the spatial extent of the computation, while the shore slope served as the independent variable for estimating underwater elevation. To better capture the representative shore-to-lake gradient, we estimated shore slope using a directional and robust scheme. Directional slopes were first computed along multiple orientations (eight-neighbor directions) and then rescaled within the buffer zone to match the magnitude range of a conventional 3×3-window slope map, thereby preserving directionality while reducing biases associated with single-direction calculations. Underwater elevation calculation: The water mask was treated as the initial lake surface. A simulated recession process was then applied, progressively lowering the water level and reducing the water mask coverage. This simulation process, initially proposed by Zhu et al. (2019), has been applied in recent studies. However, previous studies required manual predefinition of the water level drop at each step. In this study, the process was improved to automatically simulate the entire recession without manual intervention. A detailed description of the simulation process is provided in Section 2.2.2. At each step of the simulated retreat, elevation values for newly exposed underwater pixels were calculated. These elevations were estimated using a new profile-based underwater elevation model. This model adopts a quadratic function as the base form and defines an assumed lowest point based on the relative slopes of the two banks. Closed-form expressions then described slope and elevation variations on both sides of this point, remaining applicable throughout the iterative drawdown. This iterative process continued until all pixels within the original water mask were assigned updated elevation values. Consequently, the original water surface elevations in the DEM were progressively replaced with estimated underwater elevations. Lake volume estimation: The updated DEM, containing elevation values for underwater pixels, was combined with the lake extent to generate a complete bathymetric map. From this map, lake depth and volume were calculated. This structured approach ensured accurate bathymetric mapping by iteratively estimating underwater elevations from shoreline topography and water level recession.

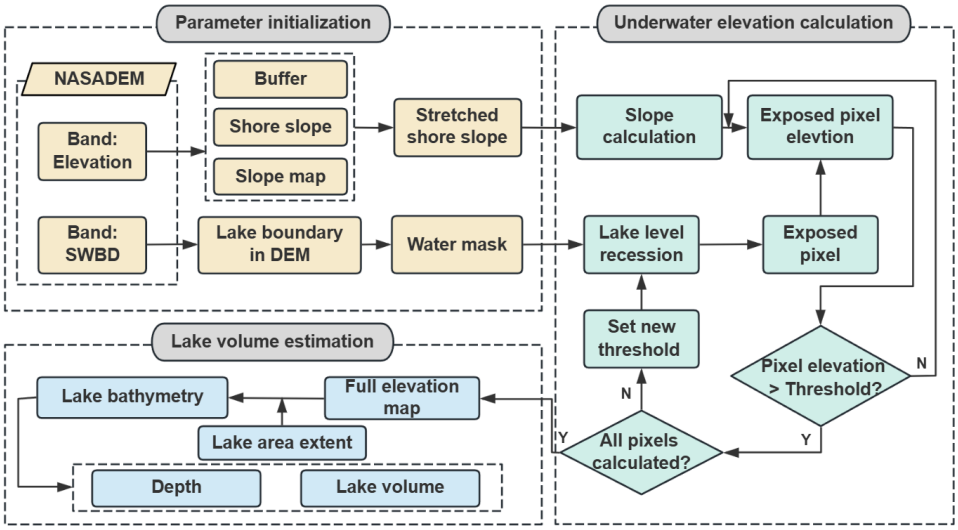

Figure 2: Flowchart of bathymetry generation and lake volume estimation.

2.2.1 Parameter initialization

The DEM dataset used in this study assigned the lake surface elevation to all water-covered pixels. To distinguish water bodies from surrounding land areas, a binary land-water classification was generated by filtering the SWBD band in the DEM, where pixels with a value of 255 denoted water. As the initial classification may contain fragmented water patches, a connected component detection algorithm was applied to eliminate these artifacts. Only the largest connected region was considered the main lake body. Once the main lake body was identified, an edge detection algorithm was employed to extract shoreline pixels. A new matrix—referred to as the water mask matrix—was then generated with the same spatial reference as the input DEM (Fig. 3b).

A multi-level buffering strategy was employed to define the spatial extent of the DEM used in subsequent calculations (Fig. 3a). A maximum buffer zone of 600 m (approximately 15–20 pixels) was established around the lake boundary in the DEM (LBD). Within this zone, nested buffer zones were generated at 100 m intervals (about 3–4 pixels). The average elevation within each buffer was calculated, producing a series of elevation values corresponding to increasing distances from the LBD.

A terrain transition point was identified by progressively sampling outward from the LBD to determine where the elevation trend shifted from increasing to decreasing. The edge at this transition point was defined as the outer edge of the final buffer extent, thereby ensuring that only terrain relevant to shoreline slope estimation was included. If no transition point was detected, the default buffer of 600 m was used.

Elevation values within the final buffer zone were used to estimate the initial shore slope. As illustrated in Fig. 3b, for each lake boundary pixel in the water mask matrix, an 8-neighborhood detection method was applied to identify adjacent land pixels in the landward direction. Using the DEM's elevation band, elevation values were extracted along this landward direction within the buffer zone (Fig. 3c). A linear or polynomial regression was then applied to estimate the slope. Once all landward slopes were computed, their average value was used as the initial shore slope, which served as a key input for underwater elevation estimation. This process was repeated for all LBD pixels.

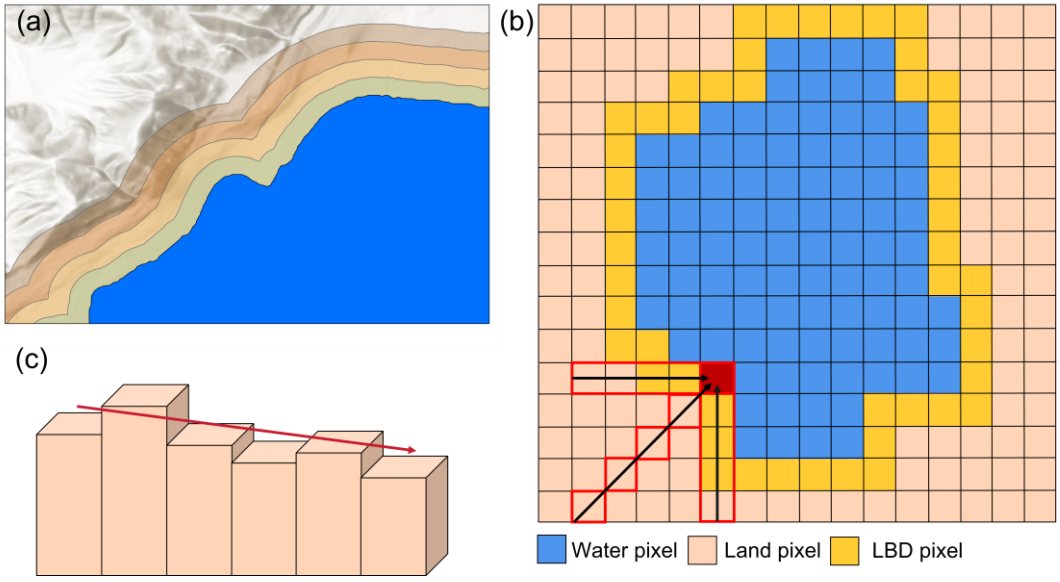

Figure 3: Shoreline slope estimation process for LBD. (a) Multi-level buffer zones surrounding the lake boundary. (b) Slope calculation using linear regression within the buffer zone. The red pixel indicates the target shoreline pixel under calculation, while the red rectangular box represents the surrounding pixels involved in the calculation. (c) Linear fitting process in a specific direction, with the red line representing the fitted slope result.

While the computed shore slope accounts for local terrain orientation, relying solely on a linear regression within a fixed window may not fully capture the elevation variability within the buffer zone. To better represent the general terrain transition from the shoreline toward the lake center, the method integrated the directional shore slope with broader topographic variation observed across the entire buffer zone. A slope map of the buffer zone was generated by applying a 3×3 moving window to estimate the slope at each pixel. This approach captured localized terrain undulations and provided a more comprehensive representation of elevation variation within the buffer. To enhance statistical robustness and reduce the influence of extreme values, outliers in the slope data were removed using a 95th-percentile threshold. The previously

computed directional shore slope values were then rescaled to match the value range of the slope map using the following transformation formula:

$$S_1'(i,j) = \min(S_2) + \frac{S_1(i,j) - \min(S_1)}{\max(S_1) - \min(S_1)} \times (\max(S_2) - \min(S_2)) , \quad (1)$$

2.2.2 Underwater elevation calculation

Based on the principle of terrain continuity, underwater areas closer to the shoreline tend to exhibit greater similarity to the topographic characteristics of the shoreline. Following this principle, the elevation values of underwater pixels near the shoreline were iteratively estimated using the following formula:

$$h_i = h_i' - d \cdot k_i, \quad (2)$$

where h_i represents the elevation of the i-th pixel, h_i' is the elevation of the adjacent land pixel, d is the distance between the two pixels, and k_i is the slope at the location of the i-th pixel. As shown in Eq. (2), calculating the elevation of the i-th pixel requires the known elevation value of a neighboring pixel (i.e., h_i') as input. Therefore, the sequence and pattern in which underwater elevations were calculated significantly influenced the final bathymetry results. This approach simulated the physical process of water level recession, gradually exposing underwater pixels. A loop-based method was then employed to iteratively calculate the elevation of these pixels following topographic gradients.

As illustrated in Fig. 4a, this process improved the simulation of lake recession. During each iteration, the lake level decreased incrementally, exposing a new set of underwater pixels. In steep regions, fewer underwater pixels were exposed per iteration due to rapid elevation changes, while in flatter areas, more pixels became exposed at once. As each pixel was exposed, its elevation was calculated sequentially, preserving spatial continuity and topographic consistency.

The first iteration began at the boundary of the water mask, where the elevations of all pixels adjacent to the shoreline were calculated. Among these newly computed pixels, the lowest elevation was identified and used as the threshold for the initial water-level drop. Once the elevation of an underwater pixel was determined, its status in the water mask was updated from water to land, indicating the transition from submerged to exposed. Following this, a new inner boundary was defined, and its elevation values were calculated. Pixels with elevation values greater than or equal to the updated threshold were retained for the next round of calculations. This iterative process continued until, within a given iteration, all calculated elevations were less than or equal to the threshold. At that point, the loop ended, and a new iteration began with an updated threshold. With each iteration, the shoreline elevations became progressively more uniform, simulating a realistic recession of the water surface. The process repeated until no water pixels remained in the water mask, at which point the entire lake bottom was assigned elevation values, and the bathymetric computation was complete.

It is essential to recognize that the underwater topography of a lake cannot be simplified as a single basin, as multiple sub-basins may exist (Fig. 4b). Therefore, in this study, no constraints were imposed during the simulation of lake recession. Once newly exposed land pixels connected to the shoreline, the lake was segmented into multiple sub-basins. The recession process was then applied to each sub-basin individually through boundary detection. This approach avoids the oversimplified assumption that all lakes consist of a single basin, instead accurately capturing the true complexity of the lakebed morphology.

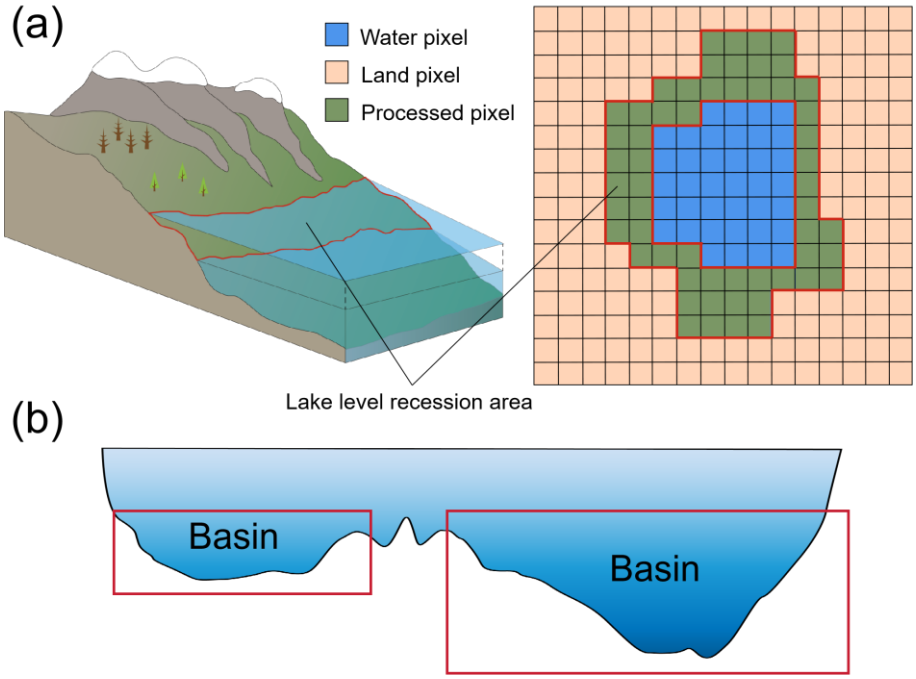

Figure 4: Simulation of the physical process of lake level recession. (a) Simulation of the physical process of lake level recession during bathymetric calculation. The red line represents the lake boundary before and after each water level drop. (b) The profile of a lake along its central axis. The red rectangle highlights the extent of the sub-basin within the lake.

During the calculation process, most water pixels were adjacent to multiple land pixels, resulting in multiple potential elevation estimates for each water pixel. To determine the most reliable elevation, a weighted average operation was applied to the estimates from each direction. The weight for each direction was based on the distance from the water pixel to the opposite shore along that direction. The specific calculation formula is as follows:

$$\begin{cases} H = \sum_{i=1}^{n} H_i \cdot w_i \\ w_i = \frac{1/d_i}{\sum_{j=1}^{n} 1/d_j} \end{cases}, \quad (3)$$

where H represents the final calculated elevation of the water pixel, H_i represents the elevation estimate from direction i, w_i represents the weight assigned to direction i, d_i represents the distance from the water pixel to the opposite shore in direction i, and n represents the total number of directions with adjacent land pixels, d_j represents the distance from a water pixel to the opposite shore in direction j, used for normalization. The final elevation of each water pixel was determined as a weighted average of estimates from all valid directions. Under the assumption that pixels closer to the shoreline provide more reliable topographic information, elevation estimates associated with shorter distances to the shore were assigned higher weights.

In Eq. (2), the parameter k_i plays a crucial role in modeling underwater topography at each pixel. It reflects the lake's cross-sectional shape, and different assumptions about this shape can significantly affect the simulation outcomes (Liu et al., 2020; Messager et al., 2016). For simplification, the method assumed that the lowest point along the lake's vertical profile could serve as the origin of a local coordinate system, as illustrated in Fig. 5. This lowest point typically lay closer to the steeper shore. To determine its position, shore slopes on both sides of the profile were first extracted. The assumed location of the lowest point was then calculated based on the relative slope values of the two shores. Taking the left shore as an example, the horizontal distance between the lowest point and the left shoreline was determined by:

$$L = D_i \cdot \frac{s_r}{s_l + s_r}, \tag{4}$$

where D_i is the total horizontal distance between the two shores along the current profile. s_l and s_r represent the slope values of the left and right shores, respectively. After determining the horizontal position of the lowest point, the model assumed that the slope at this point asymptotically approached zero, representing a local minimum in the profile. Under this assumption, the slope at the i-th pixel along the profile is assumed to decrease linearly with increasing distance from the shoreline. The slope variation is defined by the following formula:

$$k_i = s_l \cdot (1 - \frac{l}{L}), \tag{5}$$

where l represents the horizontal distance from the i-th pixel to the left shore along the profile. Although Eq. (5) provides an initial estimate of the underwater topographic slope along the profile, continuous sedimentation gradually reshapes the lakebed, leading to a progressively flatter underwater terrain.

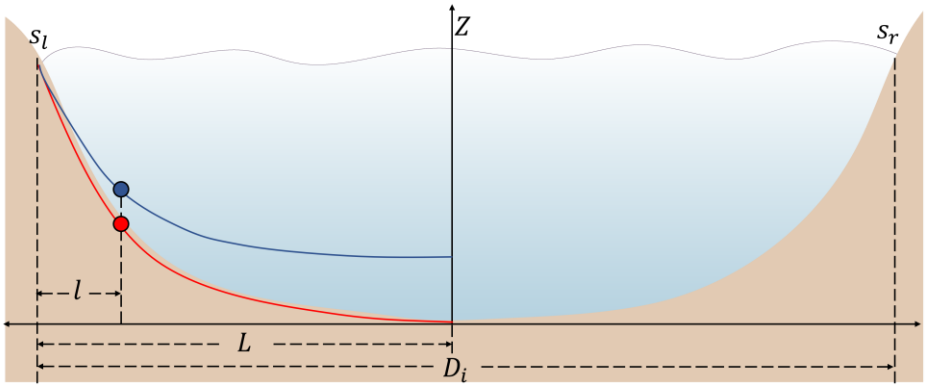

Figure 5: Schematic diagram of the lake profile coordinate system. The red line represents the lakebed profile before applying Eq. (6), while the blue line shows the profile after correction. The red and blue points indicate the positions of the calculation points along the profile before and after the correction, respectively.

To further enhance the simulation accuracy, a correction was introduced to account for sediment accumulation and its impact on underwater topography. It is assumed that sediment tends to accumulate more heavily with increasing distance from the shoreline, leading to a progressively flatter lake bottom (Håkanson, 1982). Incorporating this effect was expected to improve the realism of the simulation by aligning the modeled terrain with observed sedimentation patterns. The correction was applied to the initially estimated slope using the following formula:

$$k_i' = k_i \times \left(\frac{d_i}{D_i}\right)^{\alpha}, \tag{6}$$

where k_i' is the corrected slope at the i-th pixel, and k_i is the uncorrected slope. d_i refers to the distance from the i-th pixel on the current land boundary to the opposite shore along the profile. The exponent α reflects the influence of the surrounding terrain on sediment accumulation. To determine a representative value for α, we analyzed shoreline slope data from over 4,000 lakes on the Tibetan Plateau using the HydroLAKES dataset. The resulting distribution (Fig. S3) indicated an average shoreline slope of approximately 5.14°, which was rounded to 5° as a reference threshold for assigning the value of α. The underlying assumption is that steeper shorelines facilitate greater sediment transport toward the lake center, resulting in the formation of flat sediment layers on the lakebed (Ju et al., 2012). Accordingly, to avoid overestimating the maximum depth in steep-shoreline lakes, α is determined as follows:

$$\begin{cases} \alpha = 1, & 0^{\circ} < \bar{\theta} \leq 5^{\circ} \\ \alpha = 2, & 5^{\circ} < \bar{\theta} \end{cases}, \tag{7}$$

where $\bar{\theta}$ is the average slope within the defined buffer area, which was extracted during the "Parameter initialization" step.

2.2.3 Lake volume estimation

Following the underwater elevation calculation steps, a DEM representing the lake's underwater topography was generated within the extent defined by the water mask. It is important to note that this water mask was derived from the original DEM data and therefore reflected the lake boundary at the time the DEM was generated. To validate the accuracy of the simulated lake volume results, we used the boundary (where depth is 0) from the measured data as the lake extent. The observed boundary was overlaid onto the simulated elevation map to generate a lake depth map, from which lake depth and volume values were extracted. The formula used to estimate lake volume is as follows:

$$V = \sum v_i = \sum s_i \times depth_i, \quad (8)$$

where V is the volume of the lake, v_i is the volume of the i-th water pixel, s_i is the area of the i-th pixel (equal to the product of the pixel's length and width), and $depth_i$ is the water depth at the i-th pixel.

Since in situ bathymetric data did not include the water surface elevation at the time of measurement, a simple method was employed to extract this elevation. DEM elevation values along the observed lake boundary were extracted, and outliers were removed. The water surface elevation was then estimated by fitting the distribution of these elevation values to a Generalized Extreme Value (GEV) distribution (Tseng et al., 2016; Morrison and Smith, 2002). Once the water surface elevation was obtained, the bathymetric map was converted to elevation values by subtracting the water depth from the water surface elevation.

2.2.4 Accuracy evaluation

To assess the spatial differences between the simulated and measured water depths, 2,500 validation points were randomly selected across the surface of each lake. A linear regression analysis using the least-squares method was conducted to examine the relationship between simulated depths and in situ measurements. The evaluation metrics included the Pearson correlation coefficient (r), the normalized root-mean-square error (NRMSE), and the mean absolute error (MAE). In addition, the difference between estimated and measured lake volume was quantified using the percentage error (PE).

3 Results

3.1 Bathymetry mapping and lake volume estimates

Three-dimensional visualizations of the simulated and in situ bathymetric maps (Fig. 6) were generated to compare their spatial patterns. The results demonstrated that the simulated bathymetry closely aligned with in situ water-depth measurements, accurately capturing variations in underwater terrain. Among all the sample lakes, Dongcuo (Fig. 6c) exhibited the largest spatial discrepancy, likely due to its relatively flat shoreline, which limited the ability to infer

underwater topographic patterns from the shoreline terrain. In contrast, Ngangla Ringco (Fig. 6i), with a more complex and fragmented shoreline, introduced localized inconsistencies in the simulated topography. As a result, the model tended to overestimate depths near the shore. Furthermore, as many salt lakes have expanded significantly in recent years, a noticeable discrepancy was observed between the in situ shoreline and the DEM-derived boundary. Therefore, the bathymetry near the shoreline—derived from the DEM in the transitional area between these boundaries—was observed to be less smooth than the in situ bathymetry.

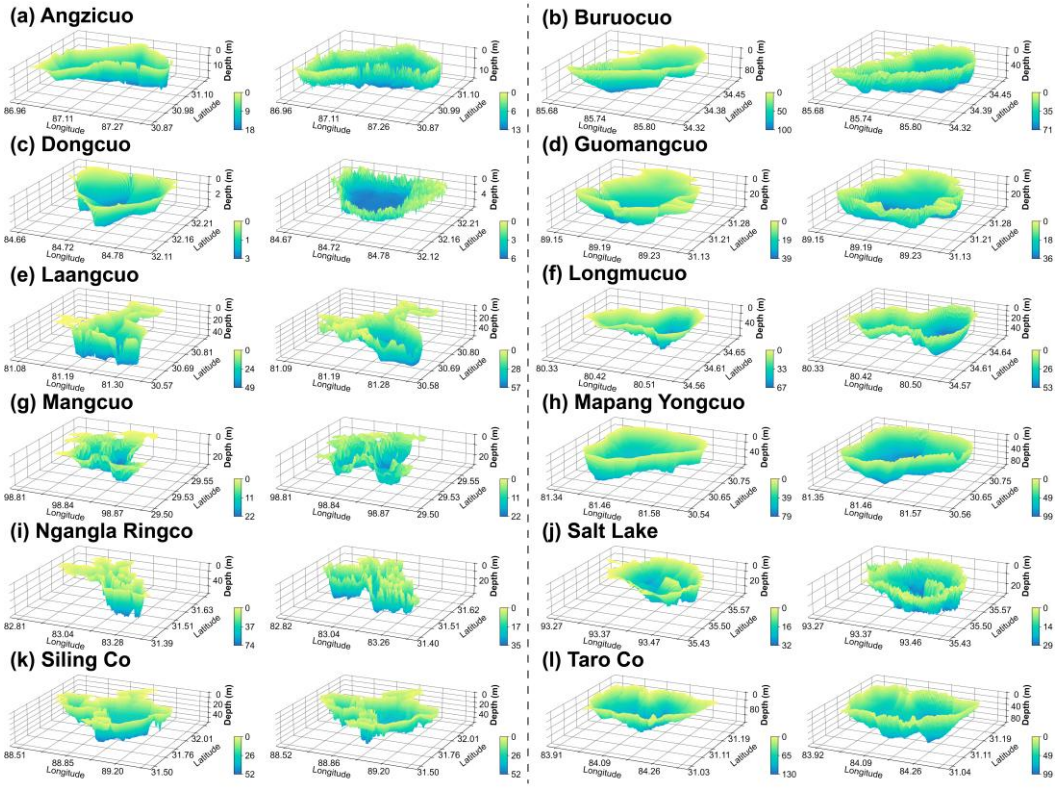

Figure 6: Three-dimensional bathymetric maps of the sample lakes, derived from in situ measurements (columns 1 and 3) and corresponding simulated results (columns 2 and 4).

To quantitatively evaluate the accuracy of the simulated bathymetry, we randomly generated 2,500 validation points within each lake boundary and compared simulated depths against in situ measurements. As shown in Fig. 7, the simulated depths exhibit good agreement with observations, with an average r value of 0.72 and an average NRMSE value of 19.09%. Because the method assumes that nearshore topography contains informative signatures of underwater slope structure, its performance depends on the signal-to-noise ratio (SNR) of shoreline-derived slope information and the degree of structural coupling between shoreline morphology and lakebed geometry within a basin.

According to Table 2, the method underestimated maximum water depth for several lakes, including Angzicuo, Buruocuo, Longmucuo, Ngangla Ringco, and Taro Co. Among them, Ngangla Ringco (Fig. 7i) shows the weakest agreement. Inspection of the three-dimensional bathymetry (Fig. 6i) reveals an abrupt deepening in the southern part of the lake, indicating a localized bathymetric anomaly and partial shoreline–lakebed decoupling. Such features are difficult to infer from shoreline terrain alone, posing a challenge for approaches that rely primarily on nearshore topographic constraints. In contrast, simulated depths were overestimated for Dongcuo and Mapang Yongcuo. In particular, Dongcuo, with a surface area of 106.80 km² and a maximum depth of 3.99 m, exhibits relatively poor simulation performance despite its shallow depth. This likely reflects the limited depth range and the heightened influence of DEM noise and subtle topographic gradients, which can reduce the robustness of shoreline-derived slope signals and amplify relative errors.

Across all lakes, MAE is strongly correlated with lake depth (r = 0.94). For deep lakes such as Buruocuo and Taro Co, where maximum water depths exceed 100 m, MAE values reached 17.33 m and 21.15 m, respectively. This pattern suggests that shoreline–lakebed coupling tends to weaken with increasing depth, consistent with a reduced ability of shoreline-derived constraints to represent deep-basin morphology. Nevertheless, the model maintains acceptable accuracy across a wide range of lake sizes, depths, and morphologies, demonstrating its general applicability for regional-scale bathymetry estimation.

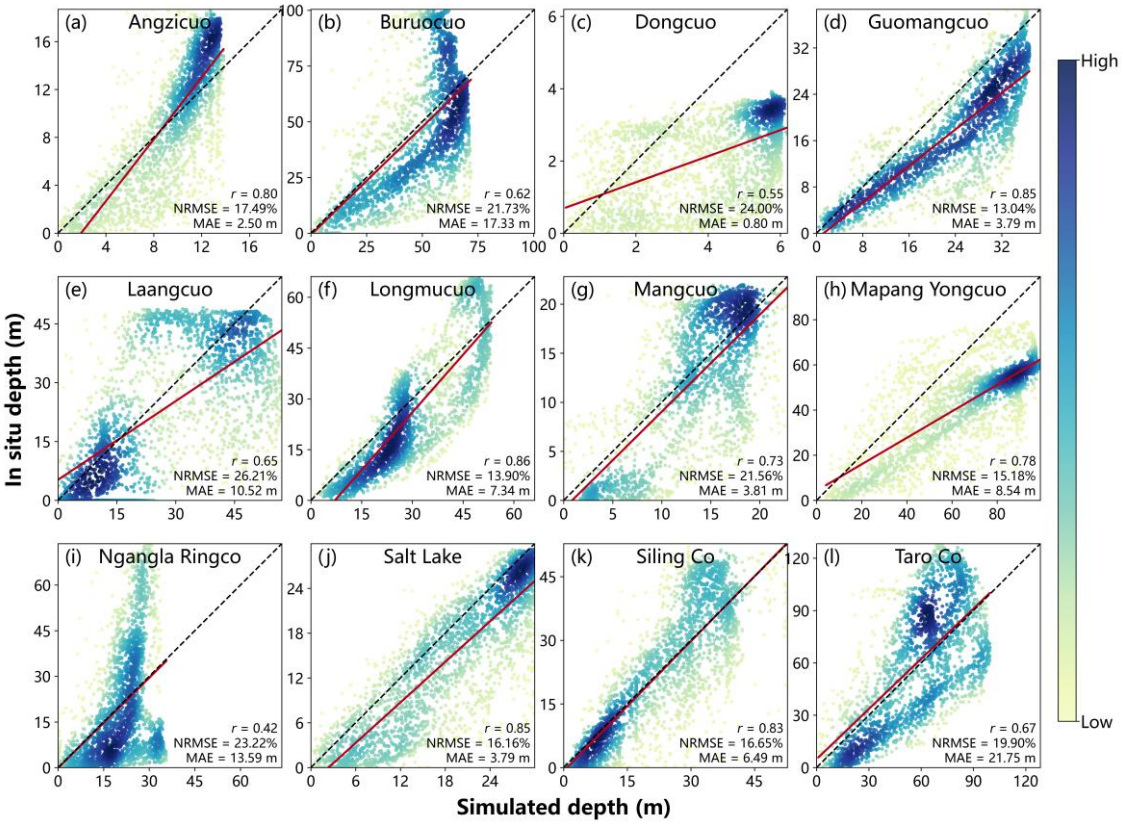

Figure 7: Scatter plots comparing simulated lake depths with in situ measurements. The dashed line represents the 1:1 line, and the red line represents the linear regression fit.

Table 2. Comparison of maximum depth and lake volume derived from in situ measurements and simulated bathymetric maps.

Lake name	Maximum depth (m)		PE*	Volume (km³)		PE
	In situ	Simulated		In situ	Simulated	
Angzicuo	18.83	13.85	-26.46%	4.81	4.65	-3.17%
Buruocuo	100.55	71.87	-28.52%	3.86	4.08	5.75%
Dongcuo	3.99	6.36	59.37%	0.22	0.43	94.84%
Guomangcuo	39.49	36.83	-6.73%	1.76	2.38	35.14%
Laangcuo	49.2	57.04	15.94%	5.53	6.41	15.81%
Longmucuo	67.52	53.45	-20.84%	2.70	3.08	14.12%
Mangcuo	22.28	22.82	2.44%	0.18	0.21	16.29%
Mapang Yongcuo	79.45	99.17	24.82%	17.20	26.70	55.22%
Ngangla Ringco	74.94	35.70	-52.37%	9.09	9.57	5.30%
Salt Lake	32.78	29.99	-8.53%	2.76	3.58	29.92%
Siling Co	52.50	53.00	0.96%	52.72	54.06	2.54%
Taro Co	130.95	99.41	-24.09%	28.02	27.01	-3.59%

*PE indicates percentage error.

Lake volume was calculated from the simulated bathymetric maps to further assess the effectiveness of the proposed method. For most lakes, the method yielded satisfactory volume estimates (Table 2). The maximum water depth was derived as the maximum pixel value in the bathymetric map. It should be noted that, in the simulated bathymetric maps, the location of the maximum depth pixel does not necessarily coincide with that in the in situ bathymetric map; nevertheless, the simulated deepest zone remains informative and provides a useful reference (Fig. S4). The PE between simulated and in situ bathymetric maps for Angzicuo, Buruocuo, Ngangla Ringco, Siling Co, and Taro Co remained within 10%. Notably, despite a substantial underestimation of the maximum depth in Ngangla Ringco, its overall lake volume estimate remained accurate. This result can be attributed to the offsetting effects between localized overestimations and underestimations in the simulated depth distribution. In contrast, Dongcuo exhibited a large discrepancy in lake volume estimation, with a PE of 94.84% compared to the volume derived from in situ bathymetry. This high error likely stemmed from the lake's shallow depth and small volume, making it highly sensitive to even minor elevation errors. Despite the underestimation of maximum depth in Angzicuo, Buruocuo, Longmucuo, and Taro Co, the volume estimates for these lakes remained reliable. This was because

the overall depth distributions across the lake surface closely matched the in situ data, as illustrated in Fig. 7. In summary, among the 12 sample lakes, 10 exhibited volume estimation errors below 30%, with eight below 20%, demonstrating that the proposed method performed well in most cases.

3.2 Validation of underwater terrain along transects

To assess the effectiveness of the proposed method for simulating underwater topography, Fig. 8 compares simulated and measured depth profiles along designated transects for 12 lakes. Each transect was carefully selected to align closely with the original depth survey routes while remaining near the lake center to ensure representative and consistent validation (Fig. S5). The average NRMSE across the 12 transects was 27.34%, and the average MAE was 10.94 m, indicating an overall acceptable level of accuracy. In general, the simulated profiles were highly consistent with in situ measurements, effectively capturing the overall trends in depth variation. When transects extended toward lake shores, the simulated elevation gradients matched the in situ measurements well, demonstrating the method's capacity to represent shoreline-to-bottom topographic transitions accurately. However, deviations were observed near the lake bottoms in several cases. Simulated depths were overestimated in Angzicuo (Fig. 8a), Buruocuo (Fig. 8b), Mangcuo (Fig. 8g), and Taro Co (Fig. 8l), while underestimations occurred in Dongcuo (Fig. 8c) and Mapang Yongcuo (Fig. 8h). In other cases—such as Longmucuo (Fig. 8f), Ngangla Ringco (Fig. 8i), and Salt Lake (Fig. 8j)—although the general profile trends aligned well with observations, the method struggled to capture localized anomalies on the lake bottom. These discrepancies are likely linked to the complex geomorphological evolution of lakes on the Tibetan Plateau, which has experienced expansion, contraction, and migration processes over time. Such dynamic processes have resulted in heterogeneous sediment deposition and irregular bathymetric features (Yu et al., 2019). Consequently, a single correction formula may not fully account for diverse lake morphologies. Despite these challenges, the proposed method demonstrated robust performance in simulating lake depth and bathymetry, supporting its applicability across varied lake environments.

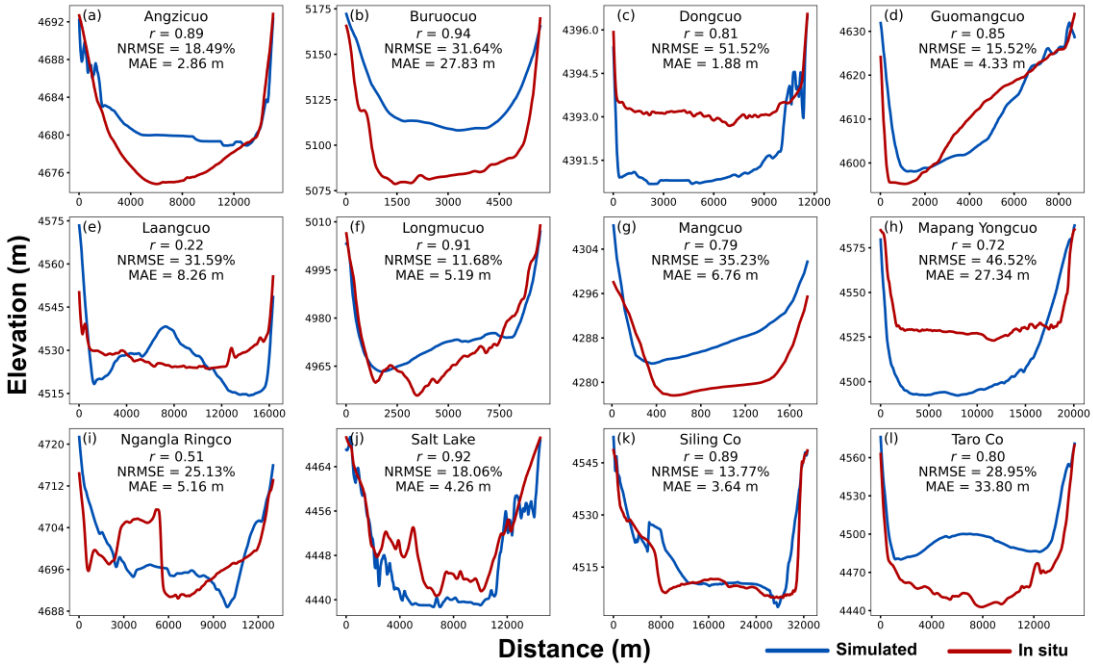

Figure 8: Elevation profiles along validation transects for each lake. Each transect was selected to closely follow the corresponding in situ survey route, providing representative comparisons between simulated and measured depths.

4. Discussion

4.1 Comparison with previous studies

The simulated lake volumes for the 12 sample lakes were compared with results from three previous studies (Table 3). For the GLOBathy dataset, absolute percentage error (APE) of lake volume estimates ranged from 1.79% to 324.93%, indicating considerable variability, with nearly half of the lakes exhibiting errors greater than 50%. In contrast, the dataset generated by Han et al. (2024) had an APE range of 0.52% to 375.20%, with four lakes showing APEs below 30%. The large errors in GLOBathy are primarily attributed to limitations in its bathymetry reconstruction method and uncertainties in estimating maximum depth. Although Han et al. (2024) proposed an ICESat-2-based bathymetry reconstruction method, their dataset was derived from empirical equations. When applied to individual lakes, these equations can introduce unpredictable errors, which can account for the observed inconsistencies. Moreover, among the nine overlapping sample lakes reported in Fang et al. (2023), the average APE was 31.80%, outperforming both GLOBathy and Han et al. (2024). In comparison, our method achieved an average APE of 27.14% across the same nine lakes. Furthermore, among all 12 sample lakes, only Dongcuo, Guomangcuo, and Mapang Yongcuo exhibited PEs greater than 30%. These findings suggest that our method provides more accurate and robust lake volume estimates compared to existing datasets.

In the comparative analysis, as the water storage estimates from Han et al. (2024) were available only through 2022, the corresponding water surface extent and water level elevation for that year were extracted, and the in situ water storage data were aligned to the same period for consistency. Since the water surface extent in GLOBathy's bathymetric maps is derived from HydroLAKES, the lake volume estimates from GLOBathy were also adjusted to reflect the conditions in 2022. It should be noted that the boundary defined by the measured bathymetric data (depth = 0 m) was considered the lake shoreline in this study. Due to limitations in the bathymetric survey equipment, measurement uncertainties may exist within the recorded depth range.

Table 3. Comparison of percentage errors (PEs) in lake volume estimates for the sample lakes across different studies.

Lake name	This study	Khazaei et al. (2022)	Han et al. (2024)	Fang et al. (2023)
Angzicuo	-3.17%	80.28%	375.20%	-24.46%
Buruocuo	5.75%	-25.52%	-82.04%	18.84%
Dongcuo	94.84%	324.93%	339.99%	63.88%
Guomangcuo	35.14%	-21.07%	-40.01%	19.47%
Laangcuo	15.81%	108.96%	29.12%	-
Longmucuo	14.12%	-47.18%	35.44%	-51.83%
Mangcuo	16.29%	1.79%	-100.00%	-
Mapang Yongcuo	55.22%	69.19%	0.52%	-36.87%
Ngangla Ringco	5.30%	-70.62%	20.98%	-
Salt Lake	29.92%	-9.73%	38.75%	1.35%
Siling Co	2.54%	15.38%	50.05%	21.36%
Taro Co	-3.59%	-34.50%	2.63%	-48.16%
Mean APE*	23.47%	67.70%	92.90%	31.80%

*APE represents the absolute percentage error.

4.2 Sensitivity to DEM resolution and buffer width

We evaluated the effects of different input DEM datasets on water depth simulation and found that the resolution and quality of the input data significantly affect the simulation errors (Fig. 9). Overall, simulations based on NASADEM achieved the lowest mean APE, followed by MERIT DEM and ALOS PALSAR. The detailed evaluation results for ALOS PALSAR and MERIT DEM are presented in Tables S1 and S2, respectively. In addition, the error distributions for NASADEM and MERIT DEM were more compact, indicating greater stability compared to the more dispersed errors observed with ALOS PALSAR-derived results. While increasing DEM resolution from 90 m to 30 m led to a clear improvement in simulation accuracy, further refinement to 12.5 m using ALOS PALSAR unexpectedly resulted in decreased accuracy. Although recent

studies have demonstrated the high vertical accuracy of ALOS PALSAR over the Tibetan Plateau (Xu et al., 2024), its performance in water depth simulation within our methodological framework was inferior to that of NASADEM. This discrepancy may be attributed to a combination of the intrinsic data quality and the simulation algorithm's sensitivity to varying spatial resolutions, which together could explain the suboptimal performance of ALOS PALSAR in this context. Beyond spatial resolution, the DEM acquisition time is also critical for our method. Because the algorithm infers underwater elevations from shoreline gradients and a DEM-derived water mask, DEMs acquired at lower lake levels can preserve more exposed nearshore topography. This additional geomorphic information strengthens constraints on shoreline-slope estimation and the subsequent recession simulation. In this regard, the earlier acquisition time of NASADEM may partly explain its better performance compared to ALOS PALSAR, despite the latter's finer spatial resolution.

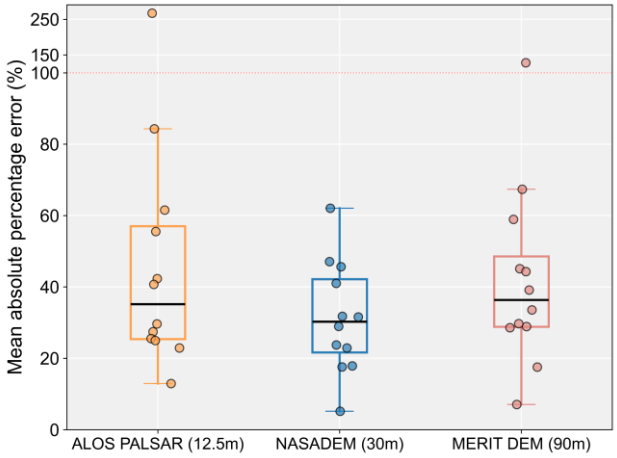

Figure 9: Box plots showing the distribution of mean absolute percentage error in lake depth simulations using three digital elevation models (DEMs) with varying spatial resolutions: ALOS PALSAR (12.5 m), NASADEM (30 m), and MERIT DEM (90 m). Each dot represents the mean absolute percentage error for an individual lake. Box ranges represent the upper and lower quartiles, and whiskers extend to 1.5 times the interquartile range. The original bathymetric survey points were selected as sample points for water depth. The data used for this figure are provided in Table S3.

We compared simulated maximum depth and volume for the 12 sample lakes using input datasets with different spatial resolutions (Table S4). Two moderately sized lakes (approximately 100 km²) with reliable simulation performance were selected to examine spatial variations in depth estimates across datasets. Overall, the bathymetric maps generated at 12.5 m (Fig. 10b, f) and 30 m resolutions (Fig. 10c, g) exhibited broadly consistent spatial patterns. In contrast, the simulated bathymetry based on the 90 m resolution DEM (Fig. 10d, h) showed a pronounced underestimation of depth across the entire domain, consistent with the quantitative depth and volume results (Table 4). This bias arises because the proposed method operates at the pixel level, and coarser resolutions smooth the shoreline elevation, leading to an underestimated slope factor during the "parameter initialization" step. Consequently, coarser-resolution inputs produce gentler underwater topography, but this results in substantial depth underestimation in deep-water areas compared with in situ measurements. Increasing the

resolution from 90 m to 30 m markedly improves the representation of deep-water areas, while further refinement to 12.5 m yields no notable change in spatial patterns. Therefore, considering both computational cost and accuracy, a 30 m input resolution is optimal for the proposed method.

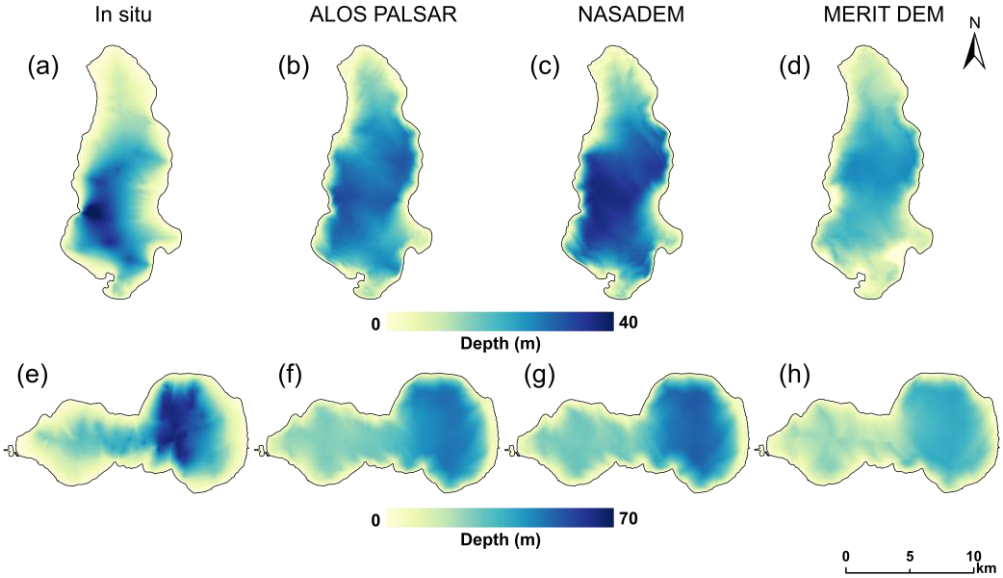

Figure 10: Comparison of simulated bathymetric maps generated using input DEMs with different spatial resolutions. Bathymetric maps for (a-d) Guomangcuo and (e-h) Longmucuo were derived from in situ data, ALOS PALSAR (12.5 m), NASADEM (30 m), and MERIT DEM (90 m), respectively.

Table 4. Comparison of simulation results using input data with different spatial resolutions.

Lake name	Input data	Maximum depth (m)	PE*	Volume (km³)	PE
Guomangcuo	ALOS PALSAR (12.5 m)	33.59	-14.92%	2.33	32.54%
	NASADEM (30 m)	36.83	-6.73%	2.38	35.14%
	MERIT DEM (90 m)	25.81	-34.64%	1.53	-13.25%
Longmucuo	ALOS PALSAR	49.96	-26.0%	2.98	10.49%
	NASADEM	53.45	-20.84%	3.08	14.12%
	MERIT DEM	39.29	-41.80%	2.33	-13.62%

*PE indicates percentage error.

We further assessed how bathymetric accuracy responds to the distance of the dynamic exposed area used to calculate shoreline slope by testing maximum buffer widths of 300, 600, and 900 m (Fig. 11). The median NRMSEs are similar across the three settings (16.65%, 18.00%, and 18.14%, respectively), indicating that overall performance is not strongly sensitive to buffer width within the tested range. However, error dispersion increases with buffer size, with the 900 m setting

exhibiting the largest interquartile range (IQR = 7.72) and a more pronounced upper tail, suggesting that overly wide buffers may incorporate broader-scale topographic signals unrelated to the representative nearshore slope (e.g., terraces or distant hillslopes), thereby degrading performance for some lakes. In contrast, the 600 m setting yields the smallest IQR (6.19) and the most consistent results across lakes; it is therefore adopted as the default in this study. Notably, because our workflow determines an adaptive buffer extent using the multi-level buffering scheme described in Section 2.2.1, the specified value represents the maximum buffer distance and is not necessarily reached for all lakes. In some cases, the optimal buffer is identified at a smaller distance, so the maximum value is not applied.

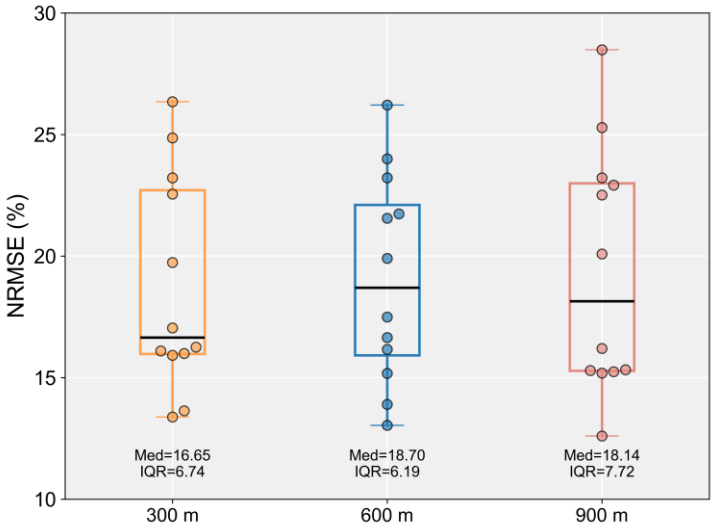

Figure 11: Boxplots of NRMSE (%) from buffer distance sensitivity experiments (300, 600, and 900 m). Box ranges represent the upper and lower quartiles, and whiskers extend to 1.5 times the interquartile range.

4.3 Method extension and applicability

To evaluate the applicability of the proposed method, we conducted a case study on Lake Mead in the United States (36.25°N, 114.39°W). As an artificial reservoir, Lake Mead differs significantly from the natural lakes analysed in this study. Being a river-type reservoir, its underwater topography exhibits significant spatial heterogeneity across different sections of the river channel. Moreover, unlike many lakes on the Tibetan Plateau, which are characterized by thick sediment layers, sediment deposition in Lake Mead is primarily concentrated within the central river channel (Fig. 12c), resulting in a relatively flat underwater terrain (Rosen and Van Metre, 2010). To account for these characteristics, the sediment correction module was applied selectively—targeting only the central portion of the profile—during simulation. This tailored approach enabled the generation of a bathymetric map for Lake Mead (Fig. 12b) that more accurately reflects its distinct geomorphological features.

The simulated underwater elevation map (Fig. 12a) showed an overall consistent pattern and morphology with the in situ bathymetric map (Fig. 12b). The error distribution was predominantly centered around zero, although localized areas of noticeable overestimation and underestimation were evident (Fig. 12c). Overestimations primarily occurred in the sediment-rich areas, which correspond to the original pre-impoundment riverbed. In these regions, applying the correction formula from Eq. (6) led to an underestimation of the slope, thereby contributing to the overestimated elevations. To quantitatively assess the simulation accuracy, 2,500 validation points were randomly selected across the entire lake, and the results were visualized in a scatter plot (Fig. 12d). The results revealed a strong correlation between in situ and simulated water depths (r = 0.66). A significant concentration of validation points was observed at elevations above 300 m, while point dispersion amplified with decreasing elevation, indicating greater uncertainty at deeper sections of the lake. Overall, simulation performance tended to degrade with increasing depth. Despite these challenges, the results demonstrate that the proposed method has promising potential for application in lakes and reservoirs across diverse environmental conditions and geomorphological settings.

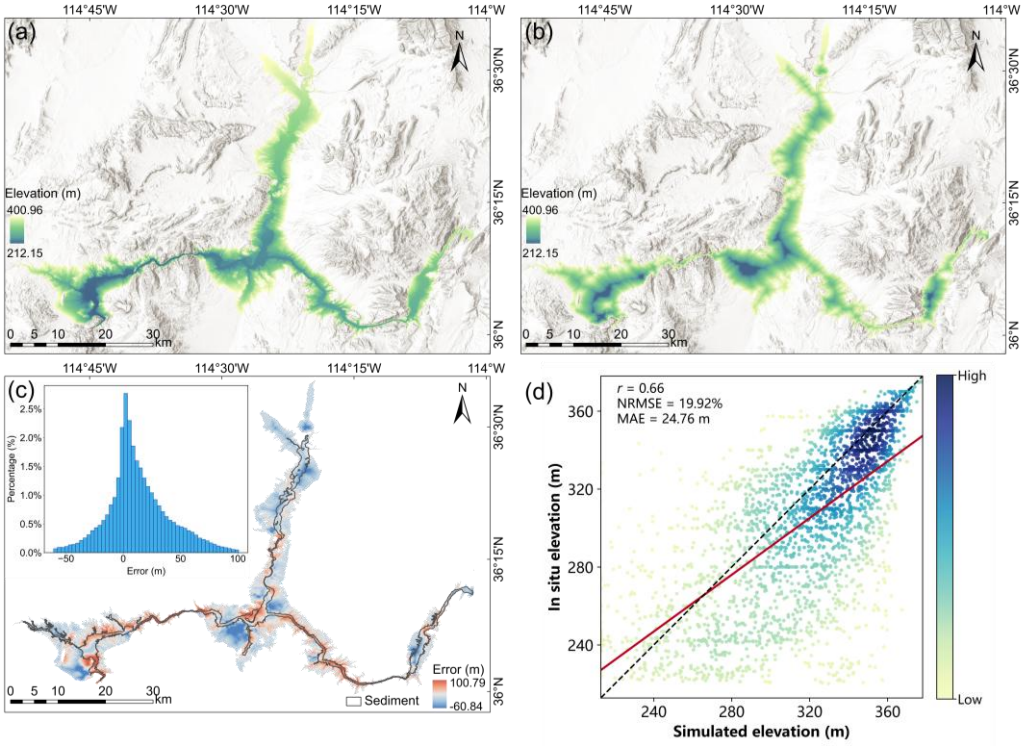

Figure 12: In situ and simulated bathymetric maps of Lake Mead, along with accuracy evaluation results. (a) In situ bathymetric map. (b) Simulated bathymetric map. (c) Error map between simulated and in situ results, accompanied by a histogram of error distribution. (d) Scatter plot comparing simulated and in situ bathymetric values.

5. Conclusion

This study presents a cost-effective method to predict underwater terrain and lake volume utilizing DEM data. The proposed approach integrates terrain continuity with lake level recession principles. Applied to 12 lakes on the Tibetan Plateau, the method demonstrates strong performance, achieving an average *r* of 0.72 and an APE of 23.47% for lake volume estimates. The simulated bathymetric maps effectively capture underwater terrain variations, providing an effective solution for reconstructing lake depth in areas lacking direct measurements. The primary source of uncertainty in the method stems from the vertical accuracy of the DEM data and error propagation during the simulation process. Since the DEM is the sole input, its quality significantly affects each simulation step. Although NASADEM has demonstrated relatively high vertical accuracy, topographic errors may still affect results, especially in large-scale applications. Furthermore, simulation errors tend to accumulate as the model progresses from the shoreline toward the lake center, explaining why depth estimates are generally more accurate near the shoreline than in the deeper central areas of the lake.

To improve accuracy and address current limitations, future efforts should focus on the integration of multi-source datasets. For example, incorporating satellite altimetry data (e.g., ICESat-2), which can partially penetrate water surfaces, could provide valuable constraints for underwater topography estimation. While satellite altimetry alone cannot fully capture underwater elevations, its integration could reduce systematic errors and mitigate the inherent shortcomings of DEM-based methods. Building on this foundation, future work will explore the use of radar-based elevation data to better represent submerged terrain and aim to develop an automated, adaptive framework for lake bathymetry estimation tailored to lake-specific characteristics. Additionally, efforts will be directed toward advancing higher-precision methods for generating lake depth maps, further enhancing the reliability of large-scale hydrological and ecological assessments.

Code availability. The codes can be accessed at: https://github.com/WangGugu64/Lake_bathymetry.

Data availability. The DEMs used in this study were obtained from publicly available datasets: (1) the ALOS PALSAR DEM provided by JAXA's Earth Observation Research Center (https://www.eorc.jaxa.jp), (2) the NASADEM distributed through NASA's Earthdata portal (https://www.earthdata.nasa.gov), and (3) the MERIT DEM developed by the University of Tokyo (https://hydro.iis.u-tokyo.ac.jp). A bathymetric map of Lake Mead was acquired from the United States Geological Survey (https://www.usgs.gov/).

Author contributions. FT: Data curation, Formal analysis, Investigation, Methodology, Validation, Visualization, Writing – original draft. YW: Formal analysis, Writing – review and editing. YJ: Writing – review and editing. XS: Writing – review and editing. SL: Writing – review and editing. YL: Conceptualization, Formal analysis, Funding acquisition, Project administration, Resources, Supervision, Writing – review and editing.

Financial support. This work was supported by the National Natural Science Foundation of China (42201349, 42571446, and 42501416), the Chongqing Municipal Science and Technology Bureau (CSTB2024YCJH-KYXM0054 and cstc2024ycjh-bgzxm0043), and the Postdoctoral Innovation Talents Support Program of Chongqing (CQBX202322).

Competing interests. The contact author has declared that none of the authors has any competing interests.

References

Cael, B. B., Heathcote, A. J., and Seekell, D. A.: The volume and mean depth of Earth's lakes, Geophys. Res. Lett., 44, 209–218, https://doi.org/10.1002/2016GL071378, 2017.

Crippen, R., Buckley, S., Agram, P., Belz, E., Gurrola, E., Hensley, S., Kobrick, M., Lavalle, M., Martin, J., Neumann, M., Nguyen, Q., Rosen, P., Shimada, J., Simard, M., and Tung, W.: NASADEM global elevation model: methods and progress, Int. Arch. Photogramm. Remote Sens. Spatial Inf. Sci., XLI-B4, 125–128, https://doi.org/10.5194/isprs-archives-XLI-B4-125-2016, 2016.

Duan, Z. and Bastiaanssen, W. G. M.: Estimating water volume variations in lakes and reservoirs from four operational satellite altimetry databases and satellite imagery data, Remote Sens. Environ., 134, 403–416, https://doi.org/10.1016/j.rse.2013.03.010, 2013.

Durand, M., Andreadis, K. M., Alsdorf, D. E., Lettenmaier, D. P., Moller, D., and Wilson, M.: Estimation of bathymetric depth and slope from data assimilation of swath altimetry into a hydrodynamic model, Geophys. Res. Lett., 35, L20401, https://doi.org/10.1029/2008GL034150, 2008.

Edmonds, D. A. and Slingerland, R. L.: Significant effect of sediment cohesion on delta morphology, Nat. Geosci., 3, 105–109, https://doi.org/10.1038/ngeo730, 2010.

Fang, C., Lu, S., Li, M., Wang, Y., Li, X., Tang, H., and Odion Ikhumhen, H.: Lake water storage estimation method based on similar characteristics of above-water and underwater topography, J. Hydrol., 618, 129146, https://doi.org/10.1016/j.jhydrol.2023.129146, 2023.

Farr, T. G., Rosen, P. A., Caro, E., Crippen, R., Duren, R., Hensley, S., Kobrick, M., Paller, M., Rodriguez, E., Roth, L., Seal, D., Shaffer, S., Shimada, J., Umland, J., Werner, M., Oskin, M., Burbank, D., and Alsdorf, D.: The Shuttle Radar Topography Mission, Rev. Geophys., 45, RG2004, https://doi.org/10.1029/2005RG000183, 2007.

Gao, H.: Satellite remote sensing of large lakes and reservoirs: from elevation and area to storage, WIREs Water, 2, 147–157, https://doi.org/10.1002/wat2.1065, 2015.

Getirana, A., Jung, H. C., and Tseng, K.-H.: Deriving three dimensional reservoir bathymetry from multi-satellite datasets, Remote Sens. Environ., 217, 366–374, https://doi.org/10.1016/j.rse.2018.08.030, 2018.

Gong, Z., Liang, S., Wang, X., and Pu, R.: Remote sensing monitoring of the bottom topography in a shallow reservoir and the spatiotemporal changes of submerged aquatic vegetation under water depth fluctuations, IEEE J. Sel. Top. Appl. Earth Obs. Remote Sens., 14, 5684–5693, https://doi.org/10.1109/JSTARS.2021.3080692, 2021.

Guo, K., Li, Q., Wang, C., Mao, Q., Liu, Y., Zhu, J., and Wu, A.: Development of a single-wavelength airborne bathymetric LiDAR: system design and data processing, ISPRS J. Photogramm. Remote Sens., 185, 62–84, https://doi.org/10.1016/j.isprsjprs.2022.01.011, 2022.

Håkanson, L.: Lake bottom dynamics and morphometry: the dynamic ratio, Water Resour. Res., 18, 1444–1450, https://doi.org/10.1029/WR018i005p01444, 1982.

Han, X., Zhang, G., Wang, J., Tseng, K.-H., Li, J., Woolway, R. I., Shum, C. K., and Xu, F.: Reconstructing Tibetan Plateau lake bathymetry using ICESat-2 photon-counting laser altimetry, Remote Sens. Environ., 315, 114458, https://doi.org/10.1016/j.rse.2024.114458, 2024.

Ju, J., Zhu, L., Feng, J., Wang, J., Wang, Y., Xie, M., Peng, P., Zhen, X., and Lü, X.: Hydrodynamic process of Tibetan Plateau lake revealed by grain size: Case study of Pumayum Co, Chin. Sci. Bull., 57, 2433–2441, https://doi.org/10.1007/s11434-012-5083-5, 2012.

Khazaei, B., Read, L. K., Casali, M., Sampson, K. M., and Yates, D. N.: GLOBathy, the global lakes bathymetry dataset, Sci. Data, 9, 36, https://doi.org/10.1038/s41597-022-01132-9, 2022.

Li, H., Zhao, J., Yan, B., Yue, L., and Wang, L.: Global DEMs vary from one to another: an evaluation of newly released Copernicus, NASA and AW3D30 DEM on selected terrains of China using ICESat-2 altimetry data, Int. J. Digit. Earth, 15, 1149–1168, https://doi.org/10.1080/17538947.2022.2094002, 2022.

Li, Y., Gao, H., Jasinski, M. F., Zhang, S., and Stoll, J. D.: Deriving high-resolution reservoir bathymetry from ICESat-2 prototype photon-counting lidar and landsat imagery, IEEE Trans. Geosci. Remote Sens., 57, 7883–7893, https://doi.org/10.1109/TGRS.2019.2917012, 2019.

Li, Y., Gao, H., Zhao, G., and Tseng, K.-H.: A high-resolution bathymetry dataset for global reservoirs using multi-source satellite imagery and altimetry, Remote Sens. Environ., 244, 111831, https://doi.org/10.1016/j.rse.2020.111831, 2020.

Li, Y., Gao, H., Allen, G. H., and Zhang, Z.: Constructing reservoir area–volume–elevation curve from TanDEM-X DEM data, IEEE J. Sel. Top. Appl. Earth Obs. Remote Sens., 14, 2249–2257, https://doi.org/10.1109/JSTARS.2021.3051103, 2021a.

Li, Y., Zhao, G., Shah, D., Zhao, M., Sarkar, S., Devadiga, S., Zhao, B., Zhang, S., and Gao, H.: NASA's MODIS/VIIRS global water reservoir product suite from moderate resolution remote sensing data, Remote Sens., 13, 565, https://doi.org/10.3390/rs13040565, 2021b.

Li, Y., Zhao, G., Allen, G. H., and Gao, H.: Diminishing storage returns of reservoir construction, Nat. Commun., 14, 3203, https://doi.org/10.1038/s41467-023-38843-5, 2023.

Liu, K. and Song, C.: Modeling lake bathymetry and water storage from DEM data constrained by limited underwater surveys, J. Hydrol., 604, 127260, https://doi.org/10.1016/j.jhydrol.2021.127260, 2022.

Liu, K., Song, C., Wang, J., Ke, L., Zhu, Y., Zhu, J., Ma, R., and Luo, Z.: Remote sensing-based modeling of the bathymetry and water storage for channel-type reservoirs worldwide, Water Resour. Res., 56, e2020WR027147, https://doi.org/10.1029/2020WR027147, 2020.

Luo, S., Song, C., Zhan, P., Liu, K., Chen, T., Li, W., and Ke, L.: Refined estimation of lake water level and storage changes on the Tibetan Plateau from ICESat/ICESat-2, Catena, 200, 105177, https://doi.org/10.1016/j.catena.2021.105177, 2021.

Messager, M. L., Lehner, B., Grill, G., Nedeva, I., and Schmitt, O.: Estimating the volume and age of water stored in global lakes using a geo-statistical approach, Nat. Commun., 7, 13603, https://doi.org/10.1038/ncomms13603, 2016.

Morrison, J. E. and Smith, J. A.: Stochastic modeling of flood peaks using the generalized extreme value distribution, Water Resour. Res., 38, 41, https://doi.org/10.1029/2001WR000502, 2002.

Pekel, J.-F., Cottam, A., Gorelick, N., and Belward, A. S.: High-resolution mapping of global surface water and its long-term changes, Nature, 540, 418–422, https://doi.org/10.1038/nature20584, 2016.

Pistocchi, A. and Pennington, D.: European hydraulic geometries for continental SCALE environmental modelling, J. Hydrol., 329, 553–567, https://doi.org/10.1016/j.jhydrol.2006.03.009, 2006.

Qiao, B., Zhu, L., Wang, J., Ju, J., Ma, Q., Huang, L., Chen, H., Liu, C., and Xu, T.: Estimation of lake water storage and changes based on bathymetric data and altimetry data and the association with climate change in the central Tibetan Plateau, J. Hydrol., 578, 124052, https://doi.org/10.1016/j.jhydrol.2019.124052, 2019.

Råman Vinnå, L., Medhaug, I., Schmid, M., and Bouffard, D.: The vulnerability of lakes to climate change along an altitudinal gradient, Commun. Earth Environ., 2, 35, https://doi.org/10.1038/s43247-021-00106-w, 2021.

Rosen, M. R. and Van Metre, P. C.: Assessment of multiple sources of anthropogenic and natural chemical inputs to a morphologically complex basin, Lake Mead, USA, Palaeogeogr. Palaeoclimatol. Palaeoecol., 294, 30–43, https://doi.org/10.1016/j.palaeo.2009.03.017, 2010.

Roy, S. and Das, B. S.: Estimation of euphotic zone depth in shallow inland water using inherent optical properties and multispectral remote sensing imagery, J. Hydrol., 612, 128293, https://doi.org/10.1016/j.jhydrol.2022.128293, 2022.

Sheffield, J., Wood, E. F., Pan, M., Beck, H., Coccia, G., Serrat-Capdevila, A., and Verbist, K.: Satellite remote sensing for water resources management: Potential for supporting sustainable development in data-poor regions, Water Resour. Res., 54, 9724–9758, https://doi.org/10.1029/2017WR022437, 2018.

Smith, W. H. F. and Sandwell, D. T.: Global Sea Floor Topography from Satellite Altimetry and Ship Depth Soundings, Science, 277, 1956–1962, https://doi.org/10.1126/science.277.5334.1956, 1997.

Song, C., Huang, B., Ke, L., and Richards, K. S.: Remote sensing of alpine lake water environment changes on the Tibetan Plateau and surroundings: A review, ISPRS J. Photogramm. Remote Sens., 92, 26–37, https://doi.org/10.1016/j.isprsjprs.2014.03.001, 2014.

Tseng, K.-H., Shum, C. K., Kim, J.-W., Wang, X., Zhu, K., and Cheng, X.: Integrating Landsat imageries and digital elevation models to infer water level change in Hoover Dam, IEEE J. Sel. Top. Appl. Earth Obs. Remote Sens., 9, 1696–1709, https://doi.org/10.1109/JSTARS.2015.2500599, 2016.

Vinogradova, N. T., Pavelsky, T. M., Farrar, J. T., Hossain, F., and Fu, L.-L.: A new look at Earth's water and energy with SWOT, Nat. Water, 3, 27–37, https://doi.org/10.1038/s44221-024-00372-w, 2025.

Wang, Y., He, X., Shanmugam, P., Bai, Y., Li, T., Wang, D., Zhu, Q., and Gong, F.: An enhanced large-scale benthic reflectance retrieval model for the remote sensing of submerged ecosystems in optically shallow waters, ISPRS J. Photogramm. Remote Sens., 210, 160–179, https://doi.org/10.1016/j.isprsjprs.2024.03.011, 2024.

Williamson, C. E., Saros, J. E., Vincent, W. F., and Smol, J. P.: Lakes and reservoirs as sentinels, integrators, and regulators of climate change, Limnol. Oceanogr., 54, 2273–2282, https://doi.org/10.4319/lo.2009.54.6_part_2.2273, 2009.

Woolway, R. I., Kraemer, B. M., Lenters, J. D., Merchant, C. J., O'Reilly, C. M., and Sharma, S.: Global lake responses to climate change, Nat. Rev. Earth Environ., 1, 388–403, https://doi.org/10.1038/s43017-020-0067-5, 2020.

Xu, W., Li, J., Peng, D., Jiang, J., Xia, H., Yin, H., and Yang, J.: Multi-source DEM accuracy evaluation based on ICESat-2 in Qinghai-Tibet Plateau, China, Int. J. Digit. Earth, 17, 2297843, https://doi.org/10.1080/17538947.2023.2297843, 2024.

Yamazaki, D., Ikeshima, D., Tawatari, R., Yamaguchi, T., O'Loughlin, F., Neal, J. C., Sampson, C. C., Kanae, S., and Bates, P. D.: A high-accuracy map of global terrain elevations, Geophys. Res. Lett., 44, 5844–5853, https://doi.org/10.1002/2017GL072874, 2017.

Yang, D., Yang, Y., and Xia, J.: Hydrological cycle and water resources in a changing world: A review, Geogr. Sustain., 2, 115–122, https://doi.org/10.1016/j.geosus.2021.05.003, 2021.

Yoon, Y., Durand, M., Merry, C. J., Clark, E. A., Andreadis, K. M., and Alsdorf, D. E.: Estimating river bathymetry from data assimilation of synthetic SWOT measurements, J. Hydrol., 464–465, 363–375, https://doi.org/10.1016/j.jhydrol.2012.07.028, 2012.

Yu, S.-Y., Colman, S. M., and Lai, Z.-P.: Late-Quaternary history of 'great lakes' on the Tibetan Plateau and palaeoclimatic implications – A review, Boreas, 48, 1–19, https://doi.org/10.1111/bor.12349, 2019.

Zhang, S., Foerster, S., Medeiros, P., de Araújo, J. C., Motagh, M., and Waske, B.: Bathymetric survey of water reservoirs in north-eastern Brazil based on TanDEM-X satellite data, Sci. Total Environ., 571, 575–593, https://doi.org/10.1016/j.scitotenv.2016.07.024, 2016.

Zhang, T., Han, W., Fang, X., Miao, Y., Zhang, W., Song, C., Wang, Y., Khatri, D. B., and Zhang, Z.: Tectonic control of a change in sedimentary environment at 10 Ma in the northeastern Tibetan Plateau, Geophys. Res. Lett., 45, 6843–6852, https://doi.org/10.1029/2018GL078460, 2018.

Zhu, S., Liu, B., Wan, W., Xie, H., Fang, Y., Chen, X., Li, H., Fang, W., Zhang, G., Tao, M., and Hong, Y.: A New Digital Lake Bathymetry Model Using the Step-Wise Water Recession Method to Generate 3D Lake Bathymetric Maps Based on DEMs, Water, 11, 1151, https://doi.org/10.3390/w11061151, 2019.